

Article

High-Power-Factor LC Series Resonant Converter Operating Off-Resonance with Inductors Elaborated with a Composed Material of Resin/Iron Powder

Josué Lara-Reyes ¹, Mario Ponce-Silva ^{1,*} , Claudia Cortés-García ¹ , Ricardo Eliu Lozoya-Ponce ², Susana Magaly Parrilla-Rubio ¹ and Alán Rafael García-García ¹

¹ Tecnológico Nacional de México-CENIDET, Cuernavaca 62490, Mexico

² Tecnológico Nacional de México-I.T., Chihuahua 31200, Mexico

* Correspondence: mario.ps@cenidet.tecnm.mx

Abstract: The most common problems with magnetic cores in high-stress applications are changes in their permeability and low saturation flux density, forcing designers to use special nanocrystalline cores, which raises the overall cost of the circuit. This paper evaluates the performance of a low-cost magnetic material composed of unsaturated polyester la mination resin COR61-AA-531EX and 200 mesh iron powder with a grain size of 74 μm , which has magnetic properties of the so-called “soft magnetic composites”, which have good magnetic characteristics in high-frequency and high-stress applications. This composite material was used for the elaboration of magnetic cores for the inductors of a resonant converter, which aims to achieve a high power factor, where in this type of application, there are large current and voltage excursions in the magnetic components that vary between high and low frequencies, being a suitable application for testing the inductors with a magnetic core of resin/iron powder. The converter was designed to operate off-resonance at different switching frequencies from 300 kHz to 800 kHz to feed a resistive load with a power output of 19 watts. The operation of the circuit was experimentally validated using a resistive load at the output, validating the theoretical analysis and achieving a power factor above 98%.

Keywords: soft magnetic composites; high-frequency magnetic components; magnetic powder cores; resonant converters; core losses



Citation: Lara-Reyes, J.; Ponce-Silva, M.; Cortés-García, C.; Lozoya-Ponce, R.E.; Parrilla-Rubio, S.M.; García-García, A.R. High-Power-Factor LC Series Resonant Converter Operating Off-Resonance with Inductors Elaborated with a Composed Material of Resin/Iron Powder. *Electronics* **2022**, *11*, 3761. <https://doi.org/10.3390/electronics11223761>

Academic Editor:
Sergio Busquets-Monge

Received: 29 September 2022

Accepted: 13 November 2022

Published: 16 November 2022

Publisher's Note: MDPI stays neutral with regard to jurisdictional claims in published maps and institutional affiliations.



Copyright: © 2022 by the authors. Licensee MDPI, Basel, Switzerland. This article is an open access article distributed under the terms and conditions of the Creative Commons Attribution (CC BY) license (<https://creativecommons.org/licenses/by/4.0/>).

1. Introduction

The development of electronic systems has been constant, with advantages in areas such as switched-mode power supply systems, electronic ballasts, filters, etc. Nowadays, designers have focused on reducing cost and size and increasing energy efficiency to achieve good use of energy and extend the life of electronic devices [1,2]. The use of new semiconductor materials for the creation of integrated circuits and other devices has made it possible to significantly reduce the size of any type of electronic system [3,4]. Regarding losses in semiconductor devices, there are soft-switching techniques that greatly reduce this drawback, allowing them to operate at high frequencies to reduce the size of passive elements [5–7]. The problems of losses due to magnetic materials are the most difficult to deal with and have led designers to try different materials in the construction of cores for the magnetic components of power converters [8–10]. Currently, the most commonly used magnetic components for high-frequency applications use ferrite, air, and nanocrystalline magnetic cores [1–13]. The problem with using ferrite cores is that they have a low saturation flux density, typically between 0.2 and 0.5 T, whereas air-core inductors have drawbacks with unwanted stray inductances, causing electromagnetic interference that can affect nearby devices [14–16]. Regarding the nanocrystalline cores, these belong to the category of the so-called “soft magnetic composites”, which have presented good magnetic properties such as high saturation flux density, high permeability, and a high

Curie temperature, in addition to being more resistant in structure compared to ferrite cores [17,18].

The problem with these nanocrystalline cores is their high cost, which causes the converter to raise its total price and does not comply with the economic saving desired by consumers [11,19]. Due to the above, in this paper, we evaluated the performance of a type of soft magnetic material composed of resin and iron powder, which presented good magnetic properties at a high frequency and was also low cost, proving to be a suitable material for the elaboration of the magnetic components of converters operating with switching frequencies above 100 kHz.

As a method for evaluating the performance of this magnetic material, the resonant converter shown in Figure 1 was implemented, operating off-resonance at different switching frequencies from 300 kHz to 800 kHz to feed a resistive load of 19 watts at the output, where the inductor “ L_a ” was built with a toroidal core made of this soft magnetic material composed of resin and iron powder. The reason the experimental tests were performed at different operating frequencies was to check if the permeability of the magnetic cores composed of resin/iron powder varied with the frequency since it is well known that one of the problems of magnetic components is the changes in the permeability of their magnetic cores in applications where high operating frequencies are required [20–22].

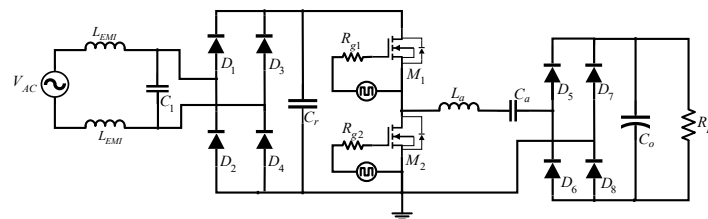


Figure 1. High power factor LC series resonant converter implemented to test the performance of magnetic cores made of resin/iron powder composite material.

To further stress the test magnetic cores, it was decided that the converter should operate off-resonance to obtain higher peak currents circulating in the resonant tank since, by operating off-resonance, the peak currents are higher compared to operating at resonance. In addition, in order to further stress the test inductor, it was decided that the proposed resonant converter would operate as a power factor corrector, which leads the circulating current in the resonant network to increase and decrease as the line voltage increases and decreases [23,24], generating higher magnetic field excursions that would saturate a conventional magnetic core [25]. Figure 2 shows the current waveform difference in the resonant network of a resonant converter with a V_{DC} source at the input and another resonant converter operating as a power factor corrector.

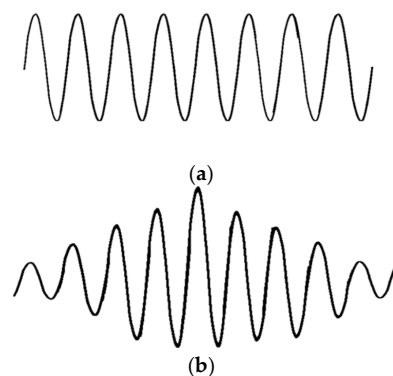


Figure 2. (a) Current in the resonant network of a resonant converter with a V_{DC} source at the input, (b) Current in the resonant network of a resonant converter with power factor correction, as shown in Figure 1.

The main contribution of this paper is to show the performance of this soft composite magnetic material in the construction of high-frequency magnetic cores to provide an option to the scientific community for selecting the appropriate material, satisfying the needs of cost, size, and energy efficiency. In addition, the analysis of this resonant converter with a high power factor operating off-resonance is presented, where the operation is first validated in a simulation and then experimentally in order to show that the established design methodology is correct.

2. Development of the Resin/Iron Powder Composite Core

2.1. Good Magnetic and Mechanical Properties

We decided to elaborate magnetic cores with this composite material of unsaturated polyester laminate resin COR61-AA-531EX and iron powder Mesh 200 with a grain size of 74 μm due to the good characteristics provided by each of these materials. Regarding the resin, this is an organic binder that presents characteristics such as excellent toughness, excellent fiberglass wet-out, high-temperature resistance, and low-laminate exothermic composition, which results in good mechanical properties (mechanical strength, plasticity, toughness) for the creation of magnetic cores in comparison with ferrite ceramic cores that are very brittle and very sensitive to temperature [26–28]. In addition, as shown in Figure 3, the resin provides insulating coatings for the iron powder particles, resulting in an increase in the electrical resistivity of the material, which greatly reduces the eddy currents in the core and provides a distributed air gap formed by binders, which reduces core saturation and increases magnetic flux density [29,30].

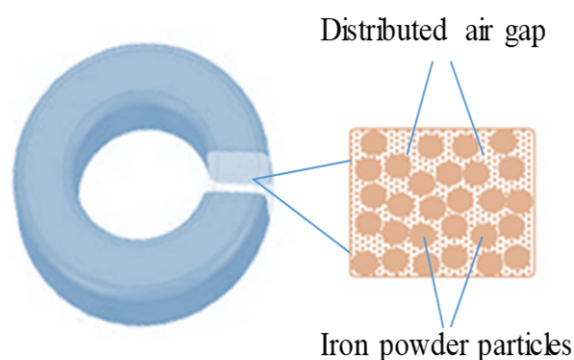


Figure 3. Proposed toroidal core with distributed air gap composed of resin and iron powder particles.

Regarding the magnetic characteristics, these are given by the iron powder particles, which are a ferromagnetic material with a grain size of 74 μm that benefits from low coercive forces that help to reduce the demagnetization fields and have narrower hysteresis cycles with lower energy losses in the core. The size of the iron powder particles is very important because if they are too small, the core will have poor fluidity and magnetic properties, and if they are too large, the compaction of the magnetic core will be difficult. A particle size between 50 and 100 μm is suitable for this type of application [31–33].

2.2. Manufacturing of the Proposed Toroidal Core

The manufacturing process consisted of using silicon molds in the shape of a toroidal core to give the size and shape to the proposed magnetic cores. The cores were manufactured with different percentages of iron powder from 55 to 85%. It was necessary to weigh the iron powder and resin to create the different cores with different percentages of iron powder. After determining the weights corresponding to each material, they were mixed with an organic binder and a catalyst to ensure uniformity, then the mixture was introduced into the silicon molds, followed by cold compaction to help form the toroidal shape. The last step was the machining process of the cores to eliminate imperfections. Figure 4 shows the cores after machining.



Figure 4. Toroidal magnetic cores elaborated with the composite material after machining.

3. Determination of the Permeability of the Magnetic Cores with the Proposed Material

After manufacturing the toroidal cores, it was necessary to determine the relative permeability of each core. For this purpose, the inductive method proposed by the ASTM A772/A772M standard for toroidal-shaped cores was applied [34]. This standard indicates that two windings must be applied to the toroidal core with the same number of turns and then an alternating current must circulate in the primary winding. Figure 5 shows the magnetic cores with the two windings already applied, and Figure 6 graphically illustrates this procedure.



Figure 5. Inductors with the same number of turns in the primary and secondary windings.

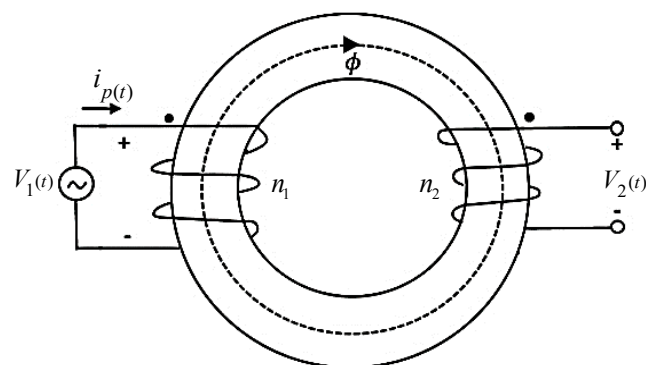


Figure 6. Proposed method with ASTM A772/A772M standard.

In order to apply the ASTM A772/A772M standard equations, it was necessary to obtain measurements of the core geometry: the magnetic path length “ L_m ” and cross-sectional area “ A_c ”. Figure 7 shows these measurements graphically; the equation to determine the length of the magnetic path is determined as follows:

$$l_m = \frac{\pi(D_o + D_i)}{2} \quad (1)$$

where D_o is the outside diameter and D_i is the inside diameter, as shown in Figure 6.



Figure 7. Required measurements for the application of the ASTM A772/ A772M standard.

As shown in Figure 6, it was necessary to generate a high-frequency sinusoidal current, which was generated by implementing the resonant inverter, as seen in Figure 8, where the inductor of the resonant network contains the test core and must be in resonance with the capacitor. The design of the resonant inverter takes into account the inductance of the primary winding of each inductor “ L_p ”, where the reactance of this inductor should be of the same value as the reactance of the capacitor “ C_p ”. The value of the resonant capacitor is determined as follows:

$$C_p = \frac{1}{\omega_o^2 L_p} \tag{2}$$

where ω_o represents the angular frequency.

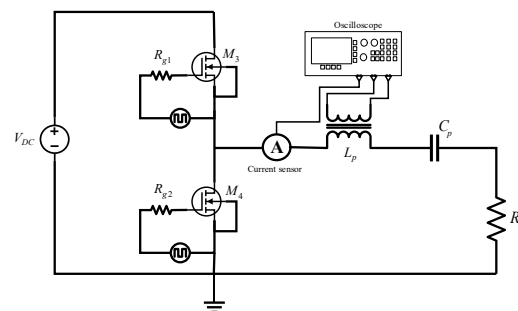


Figure 8. Implemented resonant inverter for permeability tests on elaborated cores.

In order to determine the relative permeability of the cores that were made using the ASTM A772/ A772M standard, it was necessary to do some circuit measurements such as the RMS current flowing in the primary winding and the RMS voltage induced in the secondary winding. These values were measured with a digital oscilloscope as shown in Figure 8. With the corresponding measurements, it is possible to determine the maximum magnetic flux density “ B_{max} ” and the maximum magnetic field intensity “ H_{max} ”, defined as

$$B_{max} = \frac{1}{n_2 A_c} \int_0^T V_2(t) dt \tag{3}$$

where $V_{2(t)}$ represents the voltage induced in the secondary winding.

$$H_{max} = \frac{n_1 i_p(t)}{l_m} \tag{4}$$

where $i_{p(t)}$ represents the current flowing in the primary winding.

By solving and simplifying Equations (3) and (4) in terms of RMS values, the equations indicated by the ASTM A772/ A772M standard are obtained:

$$B'_{max} = \frac{V_{RMS}}{\sqrt{2} \pi f_r n_2 A_c} \tag{5}$$

where V_{RMS} represents the RMS voltage in the secondary winding, f_r is the resonance frequency, A_c is the cross-sectional area of the core, and n_2 is the number of turns in the secondary winding.

$$H'_{max} = \frac{\sqrt{2}n_1 I_{RMS}}{l_m} \tag{6}$$

where I_{RMS} represents the RMS current in the primary winding, n_2 is the number of turns in the primary winding, and l_m is the length of the magnetic path.

Equations (5) and (6) are used to determine the relative permeability of the cores, defined as

$$\mu_r = \frac{B_{max}}{H_{max}\mu_0} \tag{7}$$

where μ_0 represents the magnetic permeability of the vacuum ($4\pi \times 10^{-7}$). Figure 9 shows the graph with the obtained values of B and H at the switching frequency of 100 kHz and 1 MHz, and Figure 10 shows the variation in the relative permeability of each core, with different percentages of iron powder in the range of switching frequencies from 100 kHz to 1 MHz. As shown in Figure 9, the resulting plots at the two switching frequencies follow a linear trend, very similar to the hysteresis plot of the air-core inductors, where the relative permeability is equal to 1 and there is no magnetic hysteresis loss due to the absence of hysteresis cycling. In addition, the linear trend shown in the graphs in Figure 9 indicates that the magnetic permeability of the cores does not vary with increasing H or frequency.

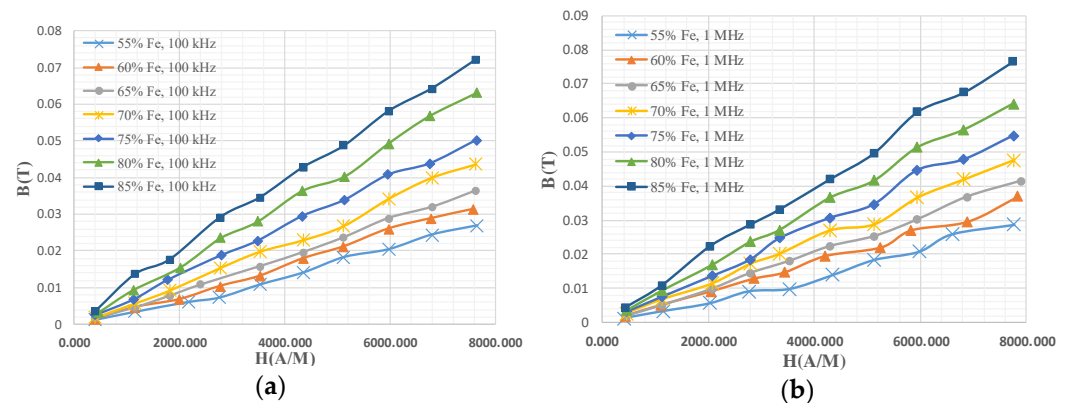


Figure 9. Graph with different values of B and H : (a) operating at a 100 kHz switching frequency, (b) operating at a 1 MHz switching frequency.

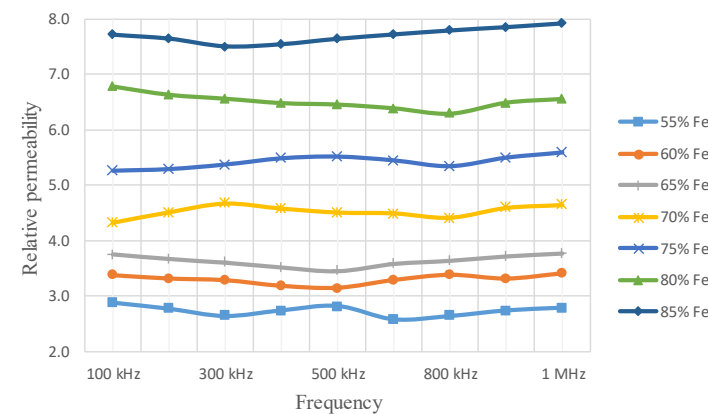


Figure 10. Relative permeability of cores made with different percentages of iron powder in the switching frequency range from 100 kHz to 1 MHz.

Figure 10 shows the variation in the relative permeability in each core operating in the switching frequency range from 100 kHz to 1 MHz. As can be seen, the relative permeability

values in each core do not vary greatly, which shows that these cores made with the resin and iron powder composite material are suitable for high-frequency applications and can be used in the construction of magnetic components of converters that operate in a switching frequency range between 100 kHz and 1 MHz.

4. Analysis of the Circuit

The first harmonic approximation (FHA) method was used for the analysis of the circuit in Figure 1, which is a modeling technique used to analyze the performance of resonant power converters, where it is assumed that only the first harmonic signal contributes to the power transfer [35,36]. This analysis has been studied and reported many times; therefore, the procedure is not included in this paper but can be found in detail in [37,38].

Power Factor Correction

In this section, the analysis of the resonant converter that achieves a high power factor operating off-resonance is developed. The circuit in Figure 11 is considered, where “ R_{eq} ” represents the equivalent of the rectifier stage, the output capacitor, and the load. The procedure to determine this equivalent resistance can be found in detail in [39] and is determined by Equation (8).

$$\frac{\pi^2 R_L}{8\eta_{req}} \tag{8}$$

where R_L represents the load at the output and η_{req} is the efficiency of the full-bridge rectifier at the output. As shown in Figure 11, the voltage that is coming out of the input rectifier is defined as

$$v_r = |V_L \sin \omega_L t| \tag{9}$$

where V_L represents the peak value of the line voltage. Figure 11 also shows the voltage that is coming out of the input rectifier that is being applied to the input of the resonant tank, defined as

$$v_{rec}(t) = \begin{cases} |V_L \sin(\omega_L t)| & 0 < t < T/2 \\ 0 & T/2 < t < T \end{cases} \tag{10}$$

where T represents the switching period of the inverter and ω_L the angular frequency of the line voltage.

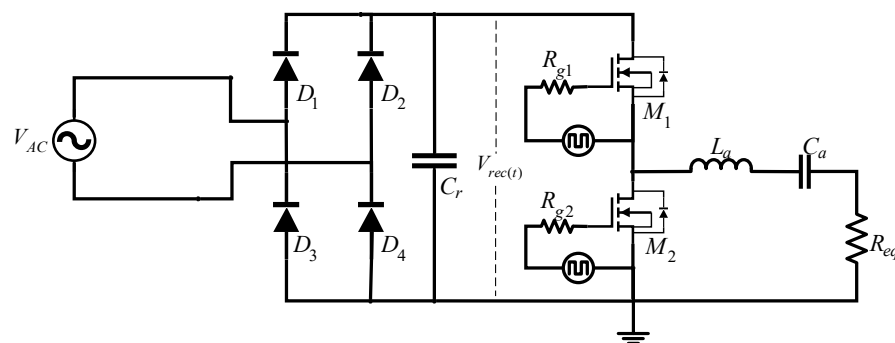


Figure 11. Equivalent circuit of the implemented resonant converter for power factor correction analysis.

The fundamental voltage at the inverter switching frequency is defined as

$$v_1 = \frac{2V_L}{\pi} |\sin \omega_L t| \sin(\omega t + \phi) \tag{11}$$

where ϕ represents the displacement angle and is defined as

$$\phi = \tan^{-1} \frac{(X_L - X_C)}{R_{eq}} \tag{12}$$

With the fundamental voltage applied to the resonant tank determined by Equation (11), a voltage divider is applied to the equivalent resistor “ R_{eq} ” determining the instantaneous current delivered by the input rectifier, defined as

$$i_{rec(t)} = \frac{2V_L}{\pi\sqrt{R_{eq}^2 + (X_L - X_C)^2}} |\sin \omega_L t| \sin(\omega t + \phi) \tag{13}$$

As the applied voltage to the resonant tank is defined by Equation (10), the instantaneous current delivered by the input rectifier “ $i_{rec(t)}$ ” is defined as

$$i_{rec(t)} = \{I_r |\sin \omega_L t| \sin(t + \phi) \quad 0 < t < T/20 \quad T/2 < t < T \tag{14}$$

where I_r represents the maximum current delivered by the input rectifier and is defined as

$$I_r = \frac{2V_L}{\pi\sqrt{R_{eq}^2 + (X_L - X_C)^2}} \tag{15}$$

Figure 12 shows the instantaneous current delivered by the rectifier “ $i_{rec(t)}$ ” and the maximum current “ I_r ”. The instantaneous power that is entering into the class D inverter is defined as

$$p_{rec(t)} = v_{rec(t)} i_{rec(t)} = \{V_L I_r |\sin \omega_L t| \sin(t + \phi) \quad 0 < t < T/20 \quad T/2 < t < T \tag{16}$$

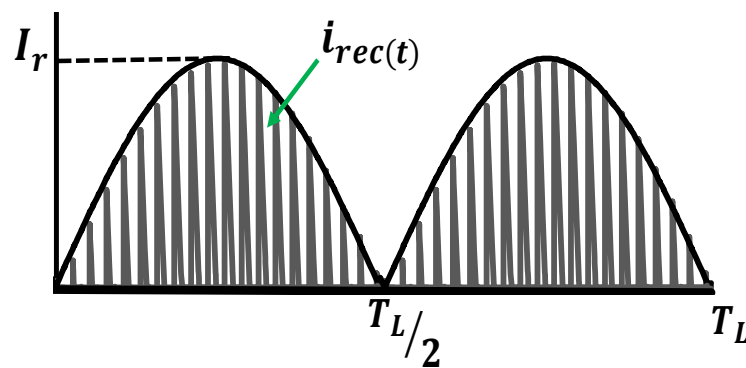


Figure 12. Instantaneous current delivered by the rectifier seen at a high frequency.

Equation (16) is integrated to find the average power in a high-frequency cycle:

$$P_{rec} = \frac{V_L I_r |\sin \omega_L t|}{2\pi} \int_0^\pi \sin(\theta + \phi) d\theta = \frac{V_L I_r |\sin \omega_L t|}{2\pi} [-\cos(\theta + \phi)]_0^\pi = \frac{V_L I_r |\sin(\omega_L t)| \cos \phi}{\pi} \tag{17}$$

From Equation (17), it is possible to obtain the average high-frequency current delivered by the rectifier, which is defined as

$$I_L = \frac{I_r \cos \phi}{\pi} \tag{18}$$

The instantaneous current delivered by the rectifier at a low frequency is defined as

$$i'_r = I_L |\sin(\omega_L t)| \tag{19}$$

Figure 13 shows the average current “ I_L ” and the instantaneous current “ i'_r ”, both in green.

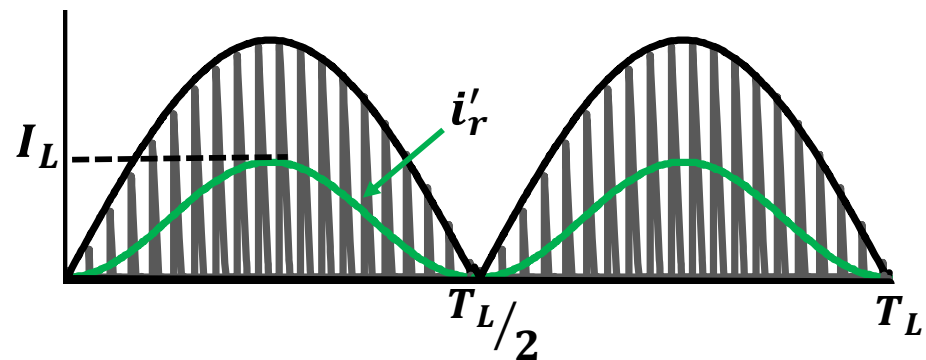


Figure 13. Instantaneous current delivered by the rectifier seen at a high frequency.

With Equations (19) and (9), it is possible to calculate the instantaneous power delivered by the rectifier at a low frequency, which is defined as

$$p_r = v_r i'_r = I_L V_L |\sin(\omega_L t)|^2 \tag{20}$$

Equation (18) is substituted in (20):

$$p_r = \frac{I_r V_L \cos \phi}{\pi} |\sin(\omega_L t)|^2 \tag{21}$$

Equation (15) is substituted in (21):

$$p_r = \frac{2V_L^2 \cos \phi}{\pi^2 \sqrt{R_{eq}^2 + (X_L - X_C)^2}} |\sin(\omega_L t)|^2 \tag{22}$$

Equation (22) is integrated to find the average power delivered by the rectifier at low frequency:

$$\begin{aligned} P_r &= \frac{2V_L^2 \cos \phi}{\pi^3 \sqrt{R_{eq}^2 + (X_L - X_C)^2}} \int_0^\pi \sin^2(\theta') d\theta' \\ &= \frac{V_L^2 \cos \phi}{\pi^3 \sqrt{R_{eq}^2 + (X_L - X_C)^2}} \left[\theta' - \frac{1}{2} \sin 2\theta' \right]_0^\pi = \frac{V_L^2 \cos \phi}{\pi^2 \sqrt{R_{eq}^2 + (X_L - X_C)^2}} \end{aligned} \tag{23}$$

where θ' is replacing $(\omega_L t)$. The apparent power coming out of the input rectifier is found. With Equation (9), the RMS voltage of the input rectifier is determined and defined as

$$\begin{aligned} V_{RMS} &= \sqrt{\frac{1}{\pi} \int_0^\pi V_L^2 \sin^2(\theta') d\theta'} = V_L \sqrt{\frac{1}{2\pi} \left[\theta' - \frac{1}{2} \sin 2\theta' \right]_0^\pi} = \\ &= \frac{V_L}{\sqrt{2}} \end{aligned} \tag{24}$$

Considering Equation (19), the RMS current of the input rectifier is determined and defined as

$$\begin{aligned} I_{RMS} &= \sqrt{\frac{1}{\pi} \int_0^\pi I_L^2 \sin^2(\theta') d\theta'} = I_L \sqrt{\frac{1}{2\pi} \left[\theta' - \frac{1}{2} \sin 2\theta' \right]_0^\pi} = \\ &= \frac{I_L}{\sqrt{2}} \end{aligned} \tag{25}$$

Equation (18) is substituted in (25):

$$I_{RMS} = \frac{I_r \cos \phi}{\sqrt{2}\pi} \tag{26}$$

The apparent power that is coming out of the input rectifier is determined by multiplying Equations (24) and (26) and is defined as follows:

$$S_r = V_{RMS} I_{RMS} = \frac{V_L I_r \cos \phi}{2\pi} \tag{27}$$

Equation (15) is substituted in (27):

$$S_r = \frac{V_L^2 \cos \phi}{\pi^2 \sqrt{R_{eq}^2 + (X_L - X_C)^2}} \tag{28}$$

Assuming 100% efficiency in the input rectifier, the power factor is expressed as follows:

$$PF = \frac{P_r}{S_r} \rightarrow \frac{\frac{V_L^2 \cos \phi}{\pi^2 \sqrt{R_{eq}^2 + (X_L - X_C)^2}}}{\frac{V_L^2 \cos \phi}{\pi^2 \sqrt{R_{eq}^2 + (X_L - X_C)^2}}} = 1 \tag{29}$$

5. Design Methodology

In order to validate the above equations, a design methodology is proposed in this work to test the operation of this converter. Table 1 shows the operating parameters of the converter for the experimental tests and Table 2 presents the proposed design methodology for a switching frequency of 500 kHz, which is verified in the simulation in Section 6.

Table 1. Design parameters for experimental tests.

| Parameter | Description | Value |
|-----------|---------------------|----------------------|
| V_{in} | Input voltage | 127 V _{RMS} |
| V_{out} | Output voltage | 27 Volts |
| P_o | Output power | 19 Watts |
| f_{sw} | Switching Frequency | 300–800 kHz |

Table 2. Design methodology for a switching frequency of 500 kHz.

| Parameter | Description | Equation | Value |
|-----------|--------------------------------------|---------------------------------------------------------------------------------------------------------------------------------------|----------|
| R_L | Load | $\frac{V_o^2}{P_o}$ | 38 Ω |
| I_o | Output current | $\frac{V_o}{R_L}$ | 720 mA |
| I_r | Maximum resonant tank current | $\frac{2V_L}{\pi \sqrt{R_{eq}^2 + (X_L - X_C)^2}}$ | 1.60 A |
| I_L | High-frequency average current | $I_r \cos \phi$ | 200 mA |
| C_r | Freewheeling capacitor | $\frac{\pi}{20V_L \omega_L}$ | 154 nF |
| n_{req} | Rectifier efficiency | $\frac{1}{1 + \frac{V_f}{V_o}}$ | 0.96 |
| R_{eq} | Equivalent resistance | $\frac{\pi^2 R_L}{8\eta_{req}}$ | 29.16 Ω |
| Q | Quality factor | $\frac{X_L}{R_{eq}}$ | 4 |
| L_1 | Complementary inductor in resonance | $\frac{QR_{eq}}{\omega_o}$ | 37 μH |
| L_{out} | Complementary off-resonance inductor | $\frac{R_{eq} \sqrt{\frac{1}{M^2} - 1}}{\omega_o}$ | 20.76 μH |
| L_a | Resonant inductor | $L_1 + L_{out}$ | 57.76 μH |
| C_a | Resonant capacitor | $\frac{1}{\omega_o^2 L_1}$ | 2.73 nF |
| PF | Power factor | $\frac{\frac{V_L^2 \cos \phi}{\pi^2 \sqrt{R_{eq}^2 + (X_L - X_C)^2}}}{\frac{V_L^2 \cos \phi}{\pi^2 \sqrt{R_{eq}^2 + (X_L - X_C)^2}}}$ | ≈100% |

6. Simulation and Experimental Results

6.1. Simulation of the Circuit

In order to validate the design methodology, the resonant converter circuit shown in Figure 1 was simulated in the software OrCAD PSpice with the values shown in Table 2. The simulation time was 500 ms, which ensures the stability of the output voltage. The simulation results are shown in Figures 14–17.

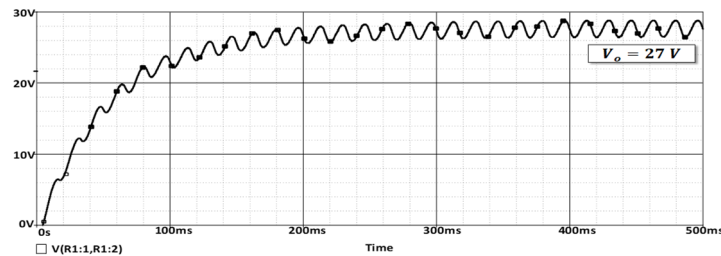


Figure 14. Output voltage plot of the resonant converter simulated in SPICE.

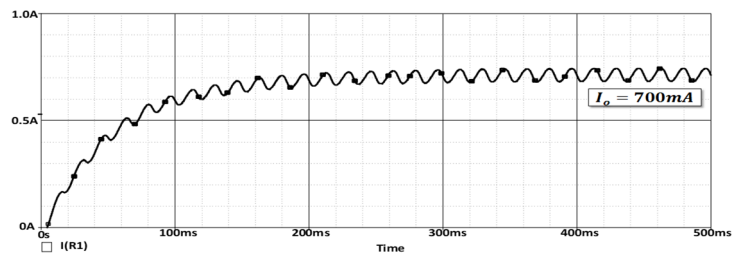


Figure 15. Output current plot of the converter simulated in SPICE.

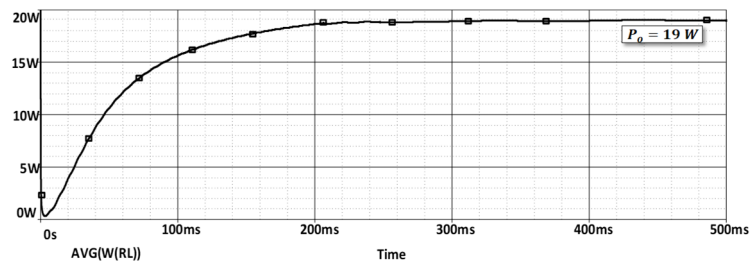


Figure 16. Output power plot of the converter simulated in SPICE.

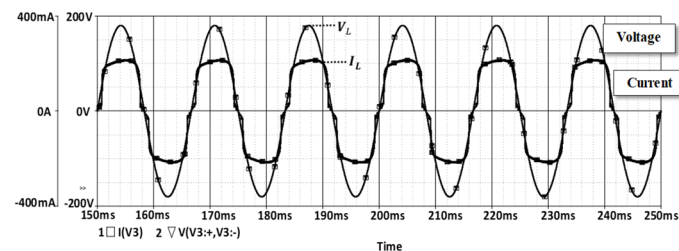


Figure 17. Voltage and current plots of the AC source at the input of the resonant converter simulated in SPICE.

Figures 14 and 15 show the output voltage and current, which present a low-frequency ripple characteristic of single-stage power-factor-correcting circuits [40,41]. Figure 16 shows the output power, which complies with the design parameter given in Table 1. Figure 17 shows the AC source voltage and current at the input of the converter, which shows that the incoming current is very close to a sinusoidal shape and is in phase with the voltage signal. In addition, Figure 17 shows the maximum current value “ I_L ” calculated in Equation (18), which coincides with the values shown in the design methodology in Table 2.

6.2. Experimental Results

The circuit in Figure 1 was implemented to experimentally validate the design methodology in Table 2 and test the performance of inductors with different magnetic cores in the resonant tank at different switching frequencies from 300 kHz to 800 kHz. Figure 18 shows the resonant converter circuit used to perform the experimental tests. For the experimental tests, current (TCP0020) and differential voltage (THDP0200) probes and a digital oscilloscope (DPO2014B) from TEKTRONIX were used.

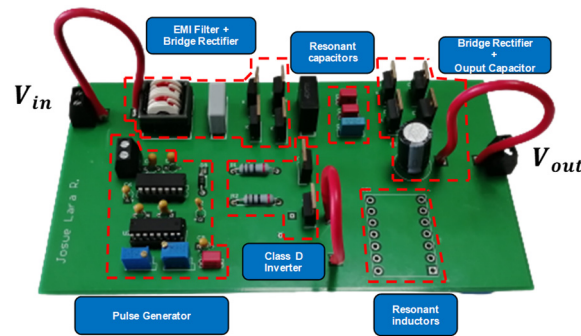


Figure 18. Experimental prototype of the circuit.

Figures 19–21 show the oscilloscope captures taken during the corresponding measurements in the experimental tests to validate the operation of the circuit. Figure 19 shows the output voltage, output current, and output power measurements, which comply with the design parameters in Table 1. These measurements show that the resonant converter is operating properly and that the design methodology established in Table 2 is correct. Figure 20 shows the input voltage and input current of the converter. As can be seen, the input current waveform is very close to a sinusoidal shape and is in phase with the voltage. This measurement shows the low distortion of the input current with which it is possible to obtain a high power factor. Figure 21 shows the waveforms corresponding to the drain-source voltage of the MOSFET M_2 and the current through the resonant tank operating off-resonance. In the experimental tests, different toroidal inductors with different magnetic cores were used to identify the power losses in the resonant tank. For this, a power subtraction was performed between the power coming out of the inverter $P_{out(inver)}$ and the power entering the output rectifier $P_{in(bridge)}$. The equation to determine the losses in the resonant tank is defined as follows:

$$P_{\text{tank}} = P_{\text{out(inver)}} - P_{\text{in(bridge)}} \tag{30}$$

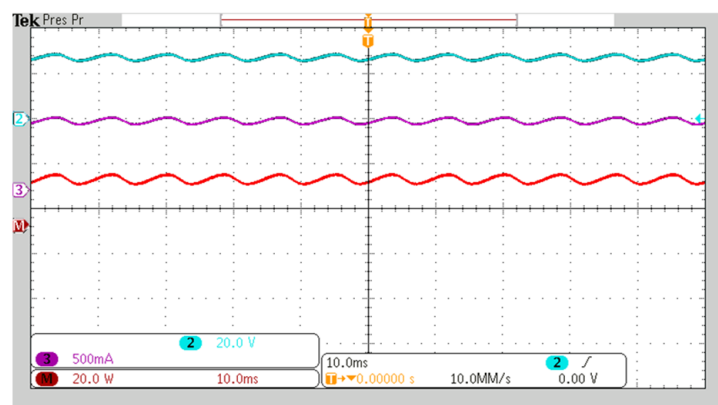


Figure 19. Waveforms: output voltage (blue, 20 V/div), output current (purple, 500 mA/div), and output power (orange, 20 W/div).

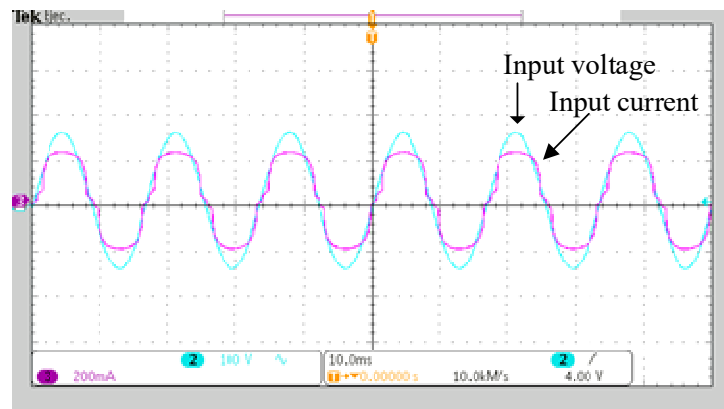


Figure 20. Waveforms: input current (purple, 200 mA/div), input voltage (blue, 100 V/div).

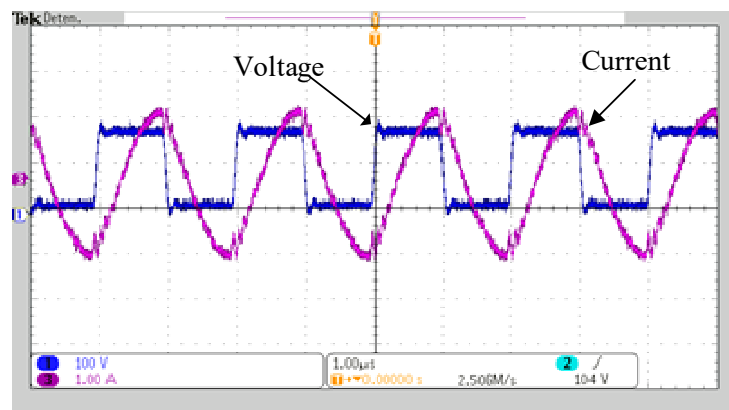


Figure 21. Waveforms: drain-source voltage (blue, 100 V/div), resonant tank current (purple, 1 A/div).

Figure 22 shows in blocks the locations where these measurements were performed in the converter. The toroidal cores used were those created with the composite material with iron powder percentages of 85%, 80%, and 75%. Since we wanted to compare the performance of these cores, they were compared with the following cores: a toroidal powder core Kool M_μ from Magnetics (Hong Kong), Ni₂Zn ferrite toroidal core from Fair-Rite, and toroidal air core, where the toroidal air core was manufactured with a mixture of organic binder and catalyst without iron powder. The dimensions of the cores correspond to those shown in Figure 7. Figure 23 shows the power losses in the resonant tank with each core operating in a switching frequency range from 300 kHz to 800 kHz with an output power of 19 watts, as established in Table 1. Figure 24 shows the variation in the converter efficiency.

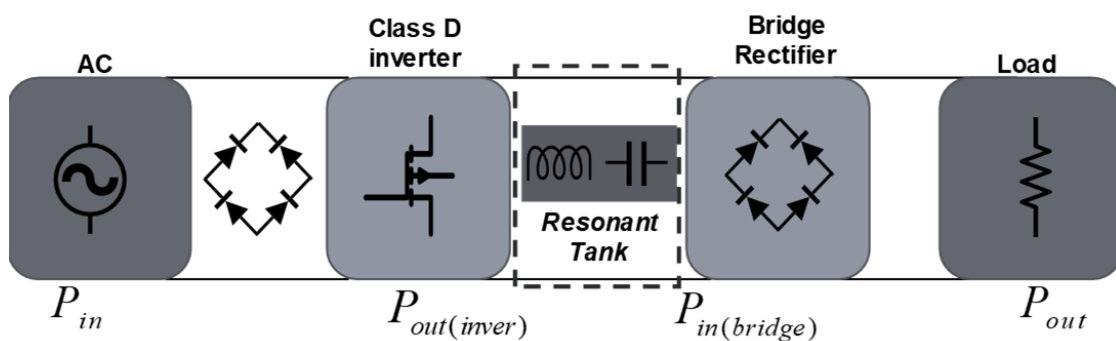


Figure 22. Block diagram of the circuit.

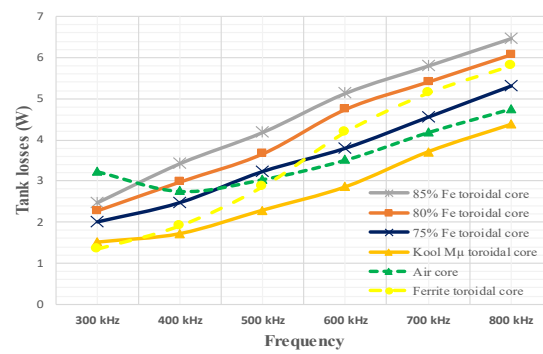


Figure 23. Power losses in the resonant tank at different switching frequencies.

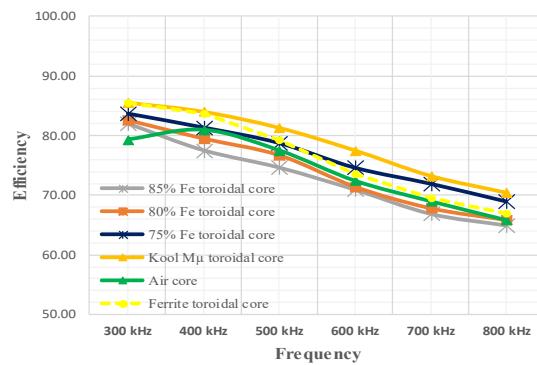


Figure 24. Efficiency in the resonant converter with inductors using different magnetic cores.

As shown in Figures 23 and 24, the magnetic core with the highest losses and lowest efficiency was the 85% iron powder core, and the core with the lowest losses and highest efficiency was the Kool Mu core from magnetics. It is interesting to see that using the core with 75% iron powder resulted in better circuit efficiency than when using the air core and also better efficiency than when using the ferrite core with a switching frequency of 600 kHz to 800 kHz. These results show that a higher percentage of iron powder in the composite material results in higher core losses, whereas in the air-core inductor, despite having no core losses, the losses increase due to stray inductances that change the required inductance, generating higher losses during switching, as well as wiring losses and parasitic capacitances that increase with the number of turns and the switching frequency. Figure 25 shows the number of turns for the required inductance at each switching frequency, where the air core needed the highest number of turns.

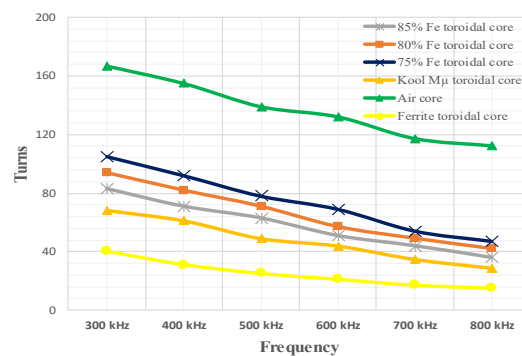


Figure 25. Number of turns in each core for the required inductance.

Other measurements were taken to evaluate the power factor and total harmonic distortion in the input current using each test core. For these measurements, the AC Power source/Analyzer 6812B from Agilent (Santa Clara, CA, USA) was used, which is

designed for applications requiring precise control, accurate measurements, and analysis of single-phase and three-phase AC power. High-power-factor values were obtained at all switching frequencies, but we decided to show the results operating at the highest switching frequency since the effect of the stray inductances in the air-core inductor was observed there, which presented the lowest power factor due to the increase in the current phase shift angle. Table 3 shows the power factor and THD levels using each core at a switching frequency of 800 kHz. As shown in Table 3, the inductors with magnetic cores made of the resin/iron powder composite material presented very similar THD and power factor values to those of the inductors with commercial ferrite and iron powder cores, avoiding unwanted stray inductances in the circuit.

Table 3. Total harmonic distortion (THD) and power factor (PF) at 800 kHz switching frequency in the input current.

| Inductor | THD | Power Factor |
|--------------|-------|--------------|
| 85% Fe | 14.46 | 98.97 |
| 80% Fe | 14.53 | 98.96 |
| 75% Fe | 14.67 | 98.94 |
| Ferrite | 14.39 | 98.98 |
| Kool M μ | 14.46 | 98.97 |
| Air | 19.50 | 98.15 |

7. Conclusions

The magnetic cores made with the resin and iron powder composite material proved to be suitable for high-frequency applications since, as shown in Figure 10, the relative permeability of the cores did not change significantly in frequency ranges from 100 kHz to 1 MHz. These cores also showed no saturation or inductance changes during the experimental tests in frequency ranges from 300 kHz to 800 kHz, complying with the design parameters of the resonant converter previously established in Table 1 and achieving high-power-factor values, as shown in Table 3, demonstrating that the design methodology and circuit analysis were correct. During the experimental tests, it was observed that a mixture of resin and 75% iron powder can be an option for the manufacturing of toroidal magnetic cores for high-frequency applications since, as shown in Figures 23 and 24, the 75% iron powder core presented better performance than the commercial ferrite core at switching frequencies from 600 kHz to 800 kHz and better performance than the air-core inductor at all switching frequencies. Therefore, it can be concluded that resin and iron powder composite cores can be an option in high-frequency applications, especially at frequencies above 600 kHz since their permeability does not vary with the frequency, they have a distributed air gap, their performance is very similar to commercial powder cores but with low-cost manufacturing, and they can replace air-core inductors since they have lower stray inductances due to higher magnetic permeability, which helps to avoid changes in the inductance of the magnetic components, avoiding inconveniences such as in the case of resonant converters, where a change in the inductance in the resonant tank generates higher switching losses due to a higher current phase shift.

Author Contributions: Conceptualization J.L.-R., M.P.-S. and S.M.P.-R.; data curation, J.L.-R., M.P.-S. and C.C.-G.; formal analysis, J.L.-R., M.P.-S., R.E.L.-P. and A.R.G.-G.; funding acquisition, M.P.-S., R.E.L.-P. and C.C.-G.; investigation, J.L.-R., M.P.-S. and S.M.P.-R.; methodology, M.P.-S., S.M.P.-R. and C.C.-G.; project administration, R.E.L.-P. and A.R.G.-G.; resources, A.R.G.-G. and M.P.-S.; software, J.L.-R. and M.P.-S.; supervision, M.P.-S. and C.C.-G.; validation, J.L.-R., M.P.-S. and R.E.L.-P.; visualization, J.L.-R. and A.R.G.-G.; writing—original draft, J.L.-R., M.P.-S. and C.C.-G.; writing—review and editing, R.E.L.-P., A.R.G.-G. and S.M.P.-R. All authors have read and agreed to the published version of the manuscript.

Funding: There was no funding for this paper.

Data Availability Statement: Not applicable.

Conflicts of Interest: The authors declare no conflict of interest.

References

1. Millan, J.; Godignon, P.; Perpina, X.; Perez-Tomas, A.; Rebollo, J. A Survey of Wide Bandgap Power Semiconductor Devices. *IEEE Trans. Power Electron.* **2013**, *29*, 2155–2163. [[CrossRef](#)]
2. Gutiérrez-Oliva, D.; Colmenar-Santos, A.; Rosales-Asensio, E. A Review of the State of the Art of Industrial Microgrids Based on Renewable Energy. *Electronics* **2022**, *11*, 1002. [[CrossRef](#)]
3. Chen, C.; Chen, Y.; Tan, Y.; Fang, J.; Luo, F.; Kang, Y. On the Practical Design of a High Power Density SiC Single-Phase Uninterrupted Power Supply System. *IEEE Trans. Ind. Inform.* **2017**, *13*, 2704–2716. [[CrossRef](#)]
4. Mortazavizadeh, S.A.; Palazzo, S.; Amendola, A.; De Santis, E.; Di Ruzza, D.; Panariello, G.; Sanseverino, A.; Velardi, F.; Busatto, G. High Frequency, High Efficiency, and High Power Density GaN-Based LLC Resonant Converter: State-of-the-Art and Perspectives. *Appl. Sci.* **2021**, *11*, 11350. [[CrossRef](#)]
5. Abbasi, M.; Lam, J. A modular SiC-based step-up converter with soft-switching-assisted networks and internally coupled high-voltage-gain modules for wind energy system with a medium-voltage DC-grid. *IEEE J. Emerg. Sel. Top. Power Electron.* **2019**, *7*, 798–810. [[CrossRef](#)]
6. Ashique, R.H.; Salam, Z.; Maruf, H.; Shihavuddin, A.; Islam, T.; Rahman, F.; Kotsampopoulos, P.; Fayek, H.H. A Comparative Analysis of Soft Switching Techniques in Reducing the Energy Loss and Improving the Soft Switching Range in Power Converters. *Electronics* **2022**, *11*, 1062. [[CrossRef](#)]
7. Ogura, K.; Chandhaket, S.; Kolhe, M.L.; Sakphrom, S.; Mekhilef, S. Simple Lossless Inductive Snubbers-Assisted Series Load Resonant Inverter Operating under ZCS-PDM Scheme for High-Frequency Induction Heating Fixed Roller. *Appl. Sci.* **2022**, *12*, 1122. [[CrossRef](#)]
8. Shen, W.; Wang, F.; Boroyevich, D.; Iv, C.W.T. High-Density Nanocrystalline Core Transformer for High-Power High-Frequency Resonant Converter. *IEEE Trans. Ind. Appl.* **2008**, *44*, 213–222. [[CrossRef](#)]
9. Simizu, S.; Ohodnicki, P.R.; McHenry, M.E. Metal Amorphous Nanocomposite Soft Magnetic Material-Enabled High Power Density, Rare Earth Free Rotational Machines. *IEEE Trans. Magn.* **2018**, *54*, 8202505. [[CrossRef](#)]
10. Liu, J.; Dong, Y.; Zhu, Z.; Zhao, H.; Pang, J.; Wang, P.; Zhang, J. Fe-Based Amorphous Magnetic Powder Cores with Low Core Loss Fabricated by Novel Gas–Water Combined Atomization Powders. *Materials* **2022**, *15*, 6296. [[CrossRef](#)] [[PubMed](#)]
11. Jiang, C.; Li, X.; Ghosh, S.S.; Zhao, H.; Shen, Y.; Long, T. Nanocrystalline Powder Cores for High-Power High-Frequency Power Electronics Applications. *IEEE Trans. Power Electron.* **2020**, *35*, 10821–10830.
12. Rodríguez-Sotelo, D.; Rodríguez-Licea, M.A.; Araujo-Vargas, I.; Prado-Olivarez, J.; Barranco-Gutiérrez, A.-I.; Perez-Pinal, F.J. Power Losses Models for Magnetic Cores: A Review. *Micromachines* **2022**, *13*, 418. [[CrossRef](#)] [[PubMed](#)]
13. Wang, D.; Zhang, J.; Cui, S.; Bie, Z.; Song, K.; Zhu, C.; Matveevich, M.I. Modern Advances in Magnetic Materials of Wireless Power Transfer Systems: A Review and New Perspectives. *Nanomaterials* **2022**, *12*, 3662. [[CrossRef](#)] [[PubMed](#)]
14. Sun, T.; Raj, P.M.; Min, J.; Wu, Z.; Sharma, H.; Takahashi, T.; Takemura, K.; Yun, H.; Carobolante, F.; Tummala, R. Magnetic Materials and Design Trade-Offs for High Inductance Density, High-Q and Low-Cost Power and EMI Filter Inductors. In Proceedings of the 2016 IEEE 66th Electronic Components and Technology Conference (ECTC), Las Vegas, NV, USA, 31 May–3 June 2016; Volume 2016, pp. 374–379. [[CrossRef](#)]
15. Meere, R.; Wang, N.; O'Donnell, T.; Kulkarni, S.; Roy, S.; O'Mathuna, S.C. Magnetic-Core and Air-Core Inductors on Silicon: A Performance Comparison up to 100 MHz. *IEEE Trans. Magn.* **2011**, *47*, 4429–4432. [[CrossRef](#)]
16. Zhang, S.; Chen, D.; Bai, B. Study of a High-Power Medium Frequency Transformer Using Amorphous Magnetic Material. *Symmetry* **2022**, *14*, 2129. [[CrossRef](#)]
17. Ruiz, D.; Ortíz, J.; Moreno, E.; Fuerte, C.; Venegas, V.; Vargas, A.; Vergara, H. Ferrites and Nanocrystalline Alloys Applied to DC–DC Converters for Renewable Energies. *Appl. Sci.* **2022**, *12*, 709. [[CrossRef](#)]
18. Zhang, X.; Han, R.; Li, F.; Pan, X.; Chu, Z. Design and Analysis of Magnetic Shielding Mechanism for Wireless Power Transfer System Based on Composite Materials. *Electronics* **2022**, *11*, 2187. [[CrossRef](#)]
19. Kauder, T.; Hameyer, K. Performance Factor Comparison of Nanocrystalline, Amorphous, and Crystalline Soft Magnetic Materials for Medium-Frequency Applications. *IEEE Trans. Magn.* **2017**, *53*, 8401504. [[CrossRef](#)]
20. Yoshida, R.; Kitajima, J.; Sakae, T.; Sato, M.; Mizuno, T.; Shimoda, Y.; Kubota, A.; Wada, S.; Kichiji, T.; Kumagai, H. Effect of Magnetic Properties of Magnetic Composite Tapes on Motor Losses. *Energies* **2022**, *15*, 7991. [[CrossRef](#)]
21. Górecki, K.; Detka, K.; Kaczerski, K. The Influence of the Transformer Core Material on the Characteristics of a Full-Bridge DC-DC Converter. *Energies* **2022**, *15*, 6160. [[CrossRef](#)]
22. Dobák, S.; Beatrice, C.; Tsakaloudi, V.; Fiorillo, F. Magnetic Losses in Soft Ferrites. *Magnetochemistry* **2022**, *8*, 60. [[CrossRef](#)]
23. Pandey, R.; Singh, B. A power-factor-corrected LLC resonant converter for electric vehicle charger using Cuk converter. *IEEE Trans. Ind. Appl.* **2019**, *55*, 6278–6286. [[CrossRef](#)]
24. Gao, W.; Gao, J.; Wu, X.; Zhou, B. Power Factor Calculation Method for the Rectifier Which AC Side Connected CRM LCL Resonant Converter. In Proceedings of the IEEE PELS Workshop on Emerging Technologies: Wireless Power Transfer (Wow), Montreal, QC, Canada, 3–7 June 2018; pp. 1–5. [[CrossRef](#)]
25. Barg, S.; Ammous, K.; Mejbri, H.; Ammous, A. An Improved Empirical Formulation for Magnetic Core Losses Estimation Under Nonsinusoidal Induction. *IEEE Trans. Power Electron.* **2016**, *32*, 2146–2154. [[CrossRef](#)]

26. Shokrollahi, H.; Janghorban, K. Soft magnetic composite materials (SMCs). *J. Mater. Process. Technol.* **2007**, *189*, 1–12. [[CrossRef](#)]
27. Sunday, K.J.; Taheri, M.L. Soft magnetic composites: Recent advancements in the technology. *Met. Powder Rep.* **2017**, *72*, 425–429. [[CrossRef](#)]
28. Hsiang, H.-I.; Wu, L.-C.; Chen, C.-C.; Lee, W.-H. Power Molding Inductors Prepared Using Amorphous FeSiCrB Alloy Powder, Carbonyl Iron Powder, and Silicone Resin. *Materials* **2022**, *15*, 3681. [[CrossRef](#)]
29. Pošković, E.; Franchini, F.; Ferraris, L. Effect of the Insulating Layer on the Properties of SMC Inductors. *Appl. Sci.* **2022**, *12*, 8756. [[CrossRef](#)]
30. Long, H.; Wu, X.; Lu, Y.; Zhang, H.; Hao, J. Effect of Polyimide-Phosphating Double Coating and Annealing on the Magnetic Properties of Fe-Si-Cr SMCs. *Materials* **2022**, *15*, 3350. [[CrossRef](#)]
31. Shokrollahi, H.; Janghorban, K. The effect of compaction parameters and particle size on magnetic properties of iron-based alloys used in soft magnetic composites. *Mater. Sci. Eng. B* **2006**, *134*, 41–43. [[CrossRef](#)]
32. Wu, Y.; Dong, Y.; Yang, M.; Jia, X.; Liu, Z.; Lu, H.; Zhang, H.; He, A.; Li, J. Effect of Annealing Process on Microstructure and Magnetic Properties of FeSiBPCNbCu Nanocrystalline Soft Magnetic Powder Cores. *Metals* **2022**, *12*, 845. [[CrossRef](#)]
33. Yan, L.; Yan, B.; Peng, L. Microstructure and Magnetic Properties of Grain Boundary Insulated Fe/Mn_{0.5}Zn_{0.5}Fe₂O₄. *Soft Magn. Compos. Mater.* **2022**, *15*, 1859.
34. *ASTM A772/A772M-00*; Standard Test Method for AC Magnetic Permeability of Materials Using Sinusoidal Current. ASTM International: West Conshohocken, PA, USA, 2016.
35. Kazimierczuk, M.K.; Czarkowski, D. *Resonant Power Converters*; John Wiley & Sons: Hoboken, NJ, USA, 2012.
36. Alatai, S.; Salem, M.; Alhamrouni, I.; Ishak, D.; Bughneda, A.; Kamarol, M. Design Methodology and Analysis of Five-Level LLC Resonant Converter for Battery Chargers. *Sustainability* **2022**, *14*, 8255. [[CrossRef](#)]
37. Wu, L.; Wang, J.; Liu, Z.; Zhang, S. Analysis and design of lc series converter considering effect of parasitic components. In Proceedings of the IEEE 2012 International Conference on Computer Distributed Control and Intelligent Environmental Monitoring, Zhangjiajie, China, 5–6 March 2012; pp. 126–130.
38. Mounika, D.; Porpandiselvi, S. ADC controlled half-bridge LC series resonant converter for LED lighting. In Proceedings of the 2017 2nd IEEE International Conference on Communication and Electronics Systems (ICCES), Coimbatore, India, 19–20 October 2017; pp. 1037–1042.
39. Erickson, R.W.; Maksimovic, D. *Fundamentals of Power Electronics*; Springer Science & Business Media: Berlin/Heidelberg, Germany, 2007.
40. Marcos-Pastor, A.; Vidal-Idiarte, E.; Cid-Pastor, A.; Martinez-Salamero, L. Minimum DC-Link Capacitance for Single-Phase Applications with Power Factor Correction. *IEEE Trans. Ind. Electron.* **2019**, *67*, 5204–5208. [[CrossRef](#)]
41. Muneer, A.; Fayyaz, A.; Iqbal, S.; Jabbar, M.W.; Qaisar, A.; Farooq, F. Single Stage Active Power Factor Correction Circuit for Street LED Light with Battery Backup. *Eng. Proc.* **2022**, *12*, 69. [[CrossRef](#)]